Revisiting the Relationship between the North Pacific High and Upwelling Winds along the West Coast of North America in the Present and Future Climate

HUI DING,[a,b] MICHAEL A. ALEXANDER,[b] AND MINGFANG TING[c]

[a] *CIRES, University of Colorado Boulder, Boulder, Colorado*
[b] *NOAA Physical Sciences Laboratory, Boulder, Colorado*
[c] *Columbia University, New York, New York*

(Manuscript received 19 April 2023, in final form 5 August 2023, accepted 21 August 2023)

ABSTRACT: The wind-driven circulation is an important driver of upwelling in the California Current System, a key factor in maintaining a productive ecosystem. In summer, the North Pacific high (NPH) dominates the atmospheric circulation, including the nearshore winds. The impact of the NPH on the surface winds along the North American west coast during summer is examined using the ECMWF Reanalysis v5 (ERA5) and the Community Earth System Model version 1 (CESM1) large ensemble of simulations. The strength, latitude, and longitude of the sea level pressure (SLP) and subsidence at 500 hPa are used to assess the NPH and its variability. While both the surface high pressure cell and subsidence are related to the interannual variability of the surface winds over the North Pacific, the strength of subsidence has a much larger effect on the coastal winds than the variability in SLP. Based on the mean of the 40 CESM simulations, future changes in upwelling also more strongly coincide with changes in subsidence than in SLP. Subsidence and southward upwelling-favorable winds increase off the Canadian coast, with the reverse occurring off the U.S. West Coast, by the end of the twenty-first century. In particular, the intermember correlation between the changes in the nearshore surface winds and the 500-hPa pressure vertical velocity reaches 0.75 and 0.87 in the southern and northern portions of the northeast Pacific, respectively. The effect of the subsidence on upwelling winds in the future is confirmed by the CESM2 large ensemble.

KEYWORDS: Anticyclones; Atmosphere-ocean interaction; Climate change

1. Introduction

The California Current System (CCS) spans the West Coast of the United States and is one of the world's major eastern boundary upwelling systems (EBUS). The CCS is located on the eastern flank of the North Pacific high (NPH, e.g., Rodwell and Hoskins 2001; Seager et al. 2003; Liu et al. 2004; Miyasaka and Nakamura 2005; Li et al. 2012; He et al. 2017) and underlies the NPH-related large-scale subsidence (e.g., Richter 2015). During summer, the equatorward ("upwelling favorable") winds prevail along a large part of North America west coast and yield extensive upwelling within ~100 km of the coast due to offshore Ekman transport since the coast is primarily meridionally oriented (e.g., Bakun 1973; Huyer 1983). The coastal upwelling is a key factor for the CCS because it delivers cold nutrient-rich water to the sunlit surface layer, providing nutrients for phytoplankton that subsequently feeds higher trophic levels (Mann and Lazier 2013). The coastal upwelling is also affected by other factors, for example, cross-shore geostrophic currents, ocean stratification, and source waters content (e.g., Jacox et al. 2018; Ding et al. 2021).

Anthropogenic climate change is expected to induce changes in coastal upwelling in the CCS and other EBUSs during summer (e.g., Bakun 1990; Brady et al. 2017). A conceptual understanding of upwelling-favorable alongshore surface winds ($\mathbf{u}_a$) is that they arise from a geostrophic balance with the local cross-shore sea level pressure (SLP) gradient, which is due to higher pressure over the ocean and a thermal low over the adjacent continent. The pressure gradient is assumed to be due to the large surface air temperature difference between the relatively cool ocean and warm continents in summer (Bakun 1973, 1975). Bakun (1990) noted a long-term trend toward an increasing cross-shore SLP gradient and therefore intensifying $\mathbf{u}_a$. The conceptual understanding inspired Bakun (1990) to attribute the trend to ongoing greenhouse gas forcing, since surface air temperature is anticipated to increase more over land than over the adjacent oceans (e.g., Manabe et al. 1991). Bakun (1990) suggested that the higher warming rate over continents would deepen the thermal low and increase the land–sea SLP gradient, inducing the intensification of $\mathbf{u}_a$ in the CCS and other EBUSs.

The potential response of $\mathbf{u}_a$ to greenhouse gas forcing has been studied extensively during the past three decades, including identifying the externally forced response from historical trends (e.g., García-Reyes et al. 2015). For the CCS, García-Reyes and Largier (2010) identified a positive trend in $\mathbf{u}_a$ during March–July over the years 1982–2008 in the central part of the California coast. Narayan et al. (2010) found an intensification of the upwelling-favorable alongshore wind stress over the years 1960–2001 along most of the California coast. Sydeman et al. (2014) conducted a meta-analysis of 22 published articles, which each used more than 20 years of observations or model output, and found significant trends

Supplemental information related to this paper is available at the Journals Online website: https://doi.org/10.1175/JCLI-D-23-0238.s1.

Corresponding author: Hui Ding, hui.ding@noaa.gov

DOI: 10.1175/JCLI-D-23-0238.1

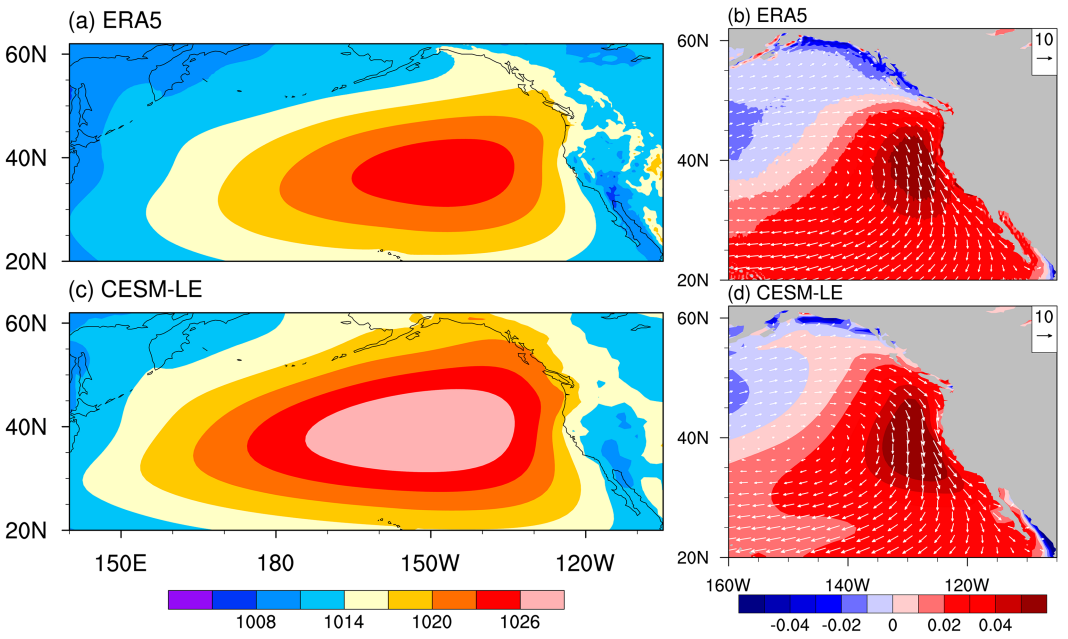

FIG. 1. Climatological mean (a),(c) sea level pressure and (b),(d) 500-hPa pressure vertical velocity (shading) and 1000-hPa wind fields (vectors) during boreal summer (JJA) calculated from (a),(b) ERA5 and (c),(d) the CESM-LE, respectively. The unit of 1000-hPa winds is m s^{-1}. The contour intervals of SLP and pressure vertical velocity are 3 hPa and 0.01 Pa s^{-1}, respectively.

of increased upwelling at higher latitudes of the CCS and other eastern boundary currents during the warm season. However, historical trends can be influenced by low-frequency variability internal to the climate system and may not be due to greenhouse gas forcing (e.g., Chhak and Di Lorenzo 2007; Brady et al. 2017).

The response of coastal upwelling in the CCS and other EBUSs to greenhouse gas forcing has been investigated using coupled atmosphere–ocean general circulation models (CGCMs; e.g., Hsieh and Boer 1992; Mote and Mantua 2002; Wang et al. 2010; Belmadani et al. 2014; Rykaczewski et al. 2015; Wang et al. 2015; Brady et al. 2017; Schmidt et al. 2020). The studies differed on the response of alongshore winds to anthropogenic climate change, and did not support Bakun's hypothesis. For example, two simulations over the years 1990–2080 were conducted using different CGCMs and neither of them showed significant changes in sea level pressure or upwelling-favorable alongshore wind stress ($\boldsymbol{\tau}_a$) in response to external forcing (Mote and Mantua 2002). A majority of CGCMs available from phase 3 of the Coupled Model Intercomparison Project (CMIP3) projected an intensified $\boldsymbol{\tau}_a$ off the coast of Oregon (Wang et al. 2010). In contrast, Wang et al. (2015) found that CMIP5 models project a strengthening of alongshore winds in the high-latitude parts of all other EBUSs (i.e., the Canary, Benguela, and Humboldt Currents) except the CCS. They further attributed the high-latitude intensification to Bakun's hypothesis, but did not investigate the deepening of the continental thermal low and the resulting intensification of the cross-shore SLP gradient. Rykaczewski et al. (2015) found that increased land–sea temperature differences were insufficient to generate increased SLP gradients and concluded that the mechanism proposed by Bakun (1990) was not the dominant process influencing anthropogenic changes in $\boldsymbol{\tau}_a$. Belmadani et al. (2014) reached a similar conclusion for the Humboldt EBUS.

As noted in previous studies (e.g., Seager et al. 2003), the North Pacific high (NPH) occupies nearly the entire North Pacific in summer. The NPH is centered in the middle of the basin (Fig. 1a), with basinwide anticyclonic circulation at the surface (Fig. S1a in the online supplemental material). On the eastern flank of the anticyclone, strong equatorward winds occur, which yield extensive coastal upwelling by offshore Ekman transport in the upper ocean (e.g., Huyer 1983). Several studies (Seager 2003; He et al. 2017) note that the NPH features large-scale subsidence in the midtroposphere, which covers a large part of the subtropical North Pacific and peaks near the coast of California (shading in Fig. 1b). The descending motion is fundamentally driven by diabatic heating of the monsoon system (Rodwell and Hoskins 2001; Karnauskas and Ummenhofer 2014). Subsidence is an indispensable component of local ocean–atmosphere coupling in the EBUSs (Richter 2015). It warms the troposphere, stabilizing the atmosphere together with the cold surface temperature below and favoring the formation of shallow stratocumulus. Further, the subsidence is also closely related to surface winds. Figure 1b shows that the equatorward winds tend to occur in the region with subsidence (Fig. 1b), consistent with Sverdrup balance $\beta v \approx f\omega$, which arises from vorticity balance in the atmosphere (Rodwell and Hoskins 2001). Here, v is the meridional velocity, ω the pressure vertical velocity, f the Coriolis force parameter, and β the derivative of

f over latitude. Links between ω and the dynamics of midlatitude atmospheric systems are examined in detail in Hoskins et al. (2003).

Previous studies have examined the link between subtropical highs and coastal upwelling in EBUSs on interannual time scales (García-Reyes et al. 2013; Schroeder et al. 2013) and on longer time scales in response to greenhouse gas forcing (Schmidt et al. 2020). Future changes in the North Pacific subtropical high during summer have been projected to occur in response to greenhouse gas forcing (Li et al. 2012; He et al. 2017). Corresponding changes in the atmospheric ridge over the Pacific–North America region can modulate the surface climate, including the temperature and precipitation over the western United States (Loikith et al. 2022). Based on CMIP5 multimodel simulations, Rykaczewski et al. (2015) found that in summer $\mathbf{u}_a$ weakened (intensified) on the equatorward (poleward) side of the four EBUSs, in response to greenhouse gas forcing. They attributed the pattern of change in $\mathbf{u}_a$ to the poleward displacement of the subtropical highs in each ocean basin. In addition, using the CESM1 large ensemble, Schmidt et al. (2020) argued that a substantial fraction of the reduced $\mathbf{u}_a$ near the California coast was explained by the externally forced trend in the NPH. These studies only considered the surface pressure when examining the impact of the subtropical highs on $\mathbf{u}_a$.

Here, we examine the impact of the NPH on $\mathbf{u}_a$ along the west coast of North America during summer (i.e., JJA) on both interannual and centennial time scales, where the latter is likely influenced by anthropogenic climate change. In addition to a SLP metric, we also define a subsidence metric to measure the NPH, since subsidence may play a critical role in relating the circulation to $\mathbf{u}_a$. We examine the potential response of the CCS upwelling to anthropogenic climate change using a large ensemble of climate model simulations. The rest of the paper is organized as follows. Section 2 describes the reanalysis dataset, model simulations, and methods used to examine internal and forced variability. In section 3, we present results on the atmospheric mean state, interannual variability of $\mathbf{u}_a$, and the externally forced changes in the subtropical high and surface winds over the North Pacific during summer. A summary and discussion are presented in section 4.

2. Data and method

a. Data and analysis method

We use monthly mean data from the European Centre for Medium-Range Weather Forecasts Reanalysis version 5 (ERA5; Hersbach et al. 2020) over the years 1979–2020, and monthly mean data from the NCAR Community Earth System Model version 1 (CESM1) large ensemble (CESM-LE; Kay et al. 2015). The CESM-LE includes 40 members, differing only slightly in their initial atmospheric conditions in January 1920. All the members are subject to the identical historical radiative forcing over the years 1920–2005 and then RCP8.5 radiative forcing over the years 2006–2100 (Riahi et al. 2011). The atmospheric model component has a horizontal resolution of approximately 1° × 1° in longitude and latitude and 30 vertical levels; the ocean model component has a horizontal resolution of approximately 1° × 1°. Data from the CESM-LE have been widely used in climate studies (e.g., Deser et al. 2016; Lovenduski et al. 2016; Brady et al. 2017; Schmidt et al. 2020).

We also examined future changes near the North America west coast, for which the CESM2 large ensemble (hereafter CESM2-LE; Danabasoglu et al. 2020) is employed. The CESM2-LE consists of 100 members covering the years 1850–2014 subject to CMIP6 historical forcing and 2015–2100 SSP370 future radiative forcing scenarios, respectively. We employed 80 members of the ensemble due to data availability. To examine future changes in the CESM2-LE, the epoch difference is calculated by comparing the later epoch over years 2071–2100 against the earlier epoch over years 1925–54, consistent with CESM-LE.

The ERA5 data are used 1) to evaluate the fidelity of the CESM-LE in simulating the present-day climate over the years 1979–2020 and then 2) to examine the impact of the NPH on the interannual variability of $\mathbf{u}_a$ along the west coast of North America. Due to data availability, surface (i.e., at a height of 10 m) winds and surface wind stress are employed from the ERA5 and the CESM-LE, respectively, when examining the impact of the NPH on the coastal upwelling. Following Brady et al. (2017), the summer mean over the years 2071–2100 from the RCP8.5 experiment is compared with that over the years 1925–54 from the historical experiment to obtain an epoch difference X^i, where i indicates ensemble member and X can be any variable of interest. Greenhouse gas forcing induced changes are given by the ensemble mean, while internal variability is obtained from the spread of the members (Kay et al. 2015; Brady et al. 2017). The signal-to-noise ratio SNR $= \overline{X}/\sigma$, where $\overline{X} = (\sum_{i=1}^{N} X^i)/N$, N is the number of ensemble members and the internal variability, and σ is given by the standard deviation of the ensemble members. For CESM-LE and CESM2-LE, N equals 40 and 80, respectively. A SNR of 2 or greater indicates that the forced change $\overline{X}$ is significant at the 95% confidence level, derived from the t test (Deser et al. 2014; Brady et al. 2017).

b. The North Pacific high metrics

We adopt two sets of metrics to measure the strength and position of the North Pacific high (NPH), which are obtained from the SLP and 500-hPa pressure vertical velocity, respectively. Hereafter, we use ω to represent pressure vertical velocity (i.e., $\omega = dP/dt$); positive ω values indicate descending motion. Each set of metrics includes strength, longitude, and latitude. The SLP metric is calculated using a method similar to Schroeder et al. (2013) and Schmidt et al. (2020). Time series of the position are given by SLP value-weighted longitude and latitude within the 1020-hPa isobar in the North Pacific bounded by 10°–60°N, 150°E–100°W: $x_t^{\mathrm{slp}} = (\sum_i^n p_t^i \times \mathrm{lon}_t^i)/\sum_i^n p_t^i$ and $y_t^{\mathrm{slp}} = (\sum_i^n p_t^i \times \mathrm{lat}_t^i)/\sum_i^n p_t^i$. Accordingly, the amplitude is given by $(\sum_i^n p_t^i)/n$, which is the SLP mean value in the same domain as the position metric. Here, lon_t^i and lat_t^i are the longitude and latitude at time t and grid cell i, p_t^i is the SLP value at $(\mathrm{lon}_t^i, \mathrm{lat}_t^i)$, and n is the total number of grid cells in the domain. Likewise, for the pressure vertical velocity metric (hereafter ω500),

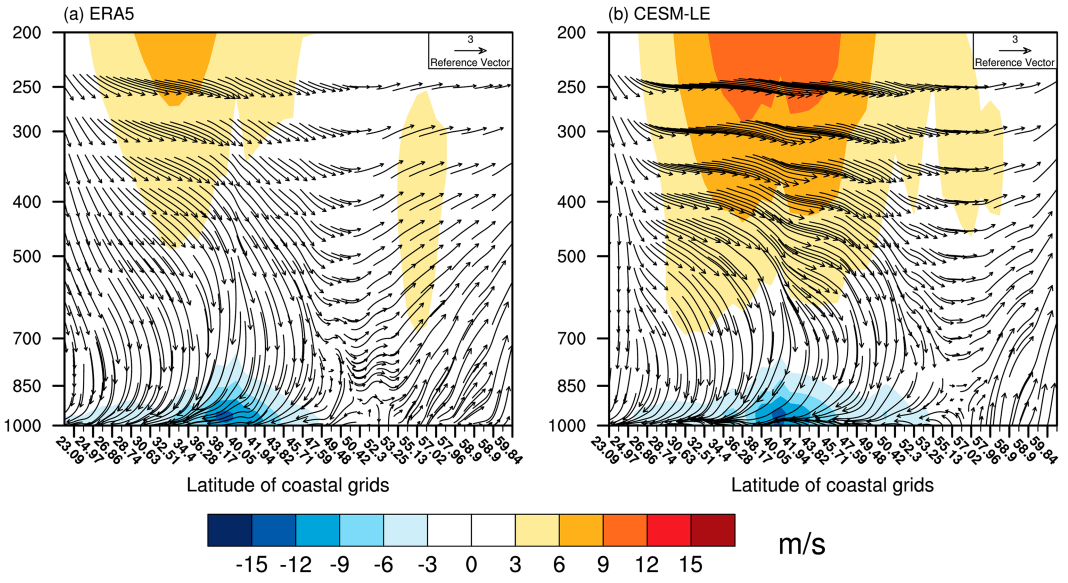

FIG. 2. The shading indicates summer mean meridional wind while vectors indicate the meridional wind together with pressure vertical velocity (omega) at a pressure and latitude along the west coast of North America, calculated from (a) ERA5 and (b) CESM-LE. In both panels, omega is scaled by $-1 \times$ [max value(v)/max value(omega)] from the ERA5, which approximately equals 106. The contour interval of the meridional wind is in m s^{-1}.

strength and position are given by $(\sum_i^n \omega_t^i \times \text{lon}_t^i)/\sum_i^n \omega_t^i$ and $(\sum_i^n \omega_t^i \times \text{lat}_t^i)/\sum_i^n \omega_t^i$ and $(\sum_i^n \omega_t^i)/n$, respectively, within the contour of 0.03 Pa s^{-1} in a domain bounded by 15°–60°N, 150°–100°W, where ω is taken from 500 hPa.

3. Results

a. *The North Pacific high and coastal winds*

A height and latitude cross section along the west coast of North America shows the relationship between meridional winds and pressure vertical velocity (vectors in Fig. 2a). Subsidence occurs in the troposphere from 200 to ~900 hPa between 20° and 50°N and then transitions to equatorward flow near the surface, consistent with the Sverdrup balance. Northerly winds are collocated with the subsidence along the coast with the maximum at about 38°N. Northerly winds occur only in a shallow layer below 800 hPa while southerly winds primarily occur above 400 hPa (shading in Fig. 2a). We obtain similar results when the cross section is taken along a fixed longitude at 130°W (Fig. S2a), which is the approximate location of the maximum subsidence at 500 hPa during summer. Thus, the NPH may modulate coastal winds via changes in large-scale subsidence.

In general, the CESM-LE accurately reproduces the summer mean atmospheric state over the Pacific–North American region including the surface high pressure cell (Fig. 1c) and atmospheric circulation in the lower troposphere (Fig. S1). However, the CESM-LE overestimates the magnitude of the surface high pressure cell by about 6 hPa (Fig. S3a). The model also captures the low over the southwestern United States. Comparing vectors in Figs. 1b and 1d indicates that the CESM-LE closely matches the observed near-surface wind fields in the coastal region adjacent to North America (Fig. S3b), despite the coarse horizontal resolution of the atmospheric model (section 2). The CESM-LE reproduces the subsidence at 500 hPa near 40°N in the eastern Pacific. One deficiency is that the descending motion in the model extends farther north than in ERA5 (Figs. 1b,d), with a positive bias centered around 50°N (Fig. S3b). The CESM-LE also reproduces the relationship between subsidence and meridional wind along the west coast (Fig. 2b) and at 130°W (Fig. S2b). The fidelity of reproducing the mean state and the relationship between subsidence and v-wind increases the confidence for examining future changes using the CESM-LE.

b. *The impact of the NPH on interannual variability of surface winds*

We examine the interannual variability of the NPH, as measured by the standard deviation of the components of the two metrics. Table 1 shows that the atmospheric high pressure cell, represented by the SLP metric, is very stable in strength and position, consistent with Schroeder et al. (2013). The standard deviation of the SLP strength is only about 0.55 hPa. In addition, the longitude and latitude components of the SLP metric have standard deviations of 2.9° and 1.1°, respectively. They indicate relatively small displacements given that the center of the NPH-related high pressure cell is in the middle of the North Pacific and located far away from the west coast of North America. Schroeder et al. (2013) also found the position of the summer high-pressure cell shifted only slightly year by year while the strength component exhibited little variability in all seasons. By contrast, the standard deviation of the strength component of the ω500 metric is 0.003 Pa s^{-1}, a substantial deviation from the summer mean (7.5%). In

TABLE 1. Climatological summer (JJA) means and standard deviations of the strength, longitude, and latitude of the SLP and the ω500 metrics of the North Pacific high. An asterisk (*) denotes 95% significance in the epoch difference (2071–2100 minus 1925–54). Positive/negative longitude (latitude) differences in the rightmost column indicate eastward/westward (northward/southward) displacement.

	ERA5		CESM-LE		
	Mean	Std dev	Mean	Std dev	Epoch difference
			SLP metric		
Strength (unit: hPa)	1022	0.55	1024	0.6	0.14
Longitude	150°W	2.9°	158°W	1.8°	−0.58°
Latitude	37°N	1.1°	39°N	1.1°	0.1°
			ω500 metric		
Strength (unit: 10^{-2} Pa s^{-1})	4	0.3	4.4	0.3	−0.2*
Longitude	131°W	1.8°	131°W	1.6°	0.18°
Latitude	34°N	1.96°	36°N	1.9°	2.4°*

addition, the position has a standard deviation of 1.8° longitude and 1.96° latitude, which represent considerable displacements given that the maximum subsidence is located next to the coast.

The two metrics are related to each other to some extent since they both represent aspects of the NPH. The correlation between the strength components of the two metrics is 0.48, which is significant at the 95% confidence level. This is because the subsidence accumulates atmospheric mass below and adds to the high pressure cell in the eastern subtropical Pacific (not shown). Likewise, the correlation between the latitude component of the two metrics is 0.64, significant at the 95% confidence level. This is because subsidence increases the surface pressure and thus the northward displacement of the subsidence results in the northward shift of the high pressure cell. By contrast, the correlation between the longitude component of the two metrics is only 0.21, which is not significant. While these two aspects of the NPH are related to some degree they may differ in their influence on surface winds along the U.S. West Coast.

To investigate how the NPH affects coastal upwelling, we calculate the correlation between surface meridional wind and the three components of the two NPH metrics using ERA5 data (Fig. 3). Several studies have adopted the meridional wind as the upwelling-favorable alongshore wind directly (e.g., Rykaczewski et al. 2015). Nevertheless, the linkage of the NPH to surface zonal wind is also shown in Fig. 4 given that zonal and meridional winds are equally efficient for inducing coastal upwelling north of ~50°N. In addition, the two NPH metrics are related to the upwelling-favorable component (Fig. S4), which is calculated by projecting the zonal and meridional winds from the first offshore grid cells onto an estimate of the angle of the coastline based on three consecutive grid cells.

We begin with the SLP metric. The strength of the NPH is only weakly correlated with northerly (upwelling-favorable) wind anomalies along the west coast with a correlation value of about −0.3 between 34° and 40°N (Fig. 3a), but has negligible impact on surface zonal wind anomalies (Fig. 4a). The strength has a modest correlation with $\mathbf{u}_a$ at the coast between 32° and 40°N, with values of about 0.3–0.4 (Fig. S4). The middle column shows that the eastward shift of the high pressure cell induces southerly wind anomalies (Fig. 3b) and easterly wind anomalies (Fig. 4b) in a small coastal region near 34°N, both of which are unfavorable for upwelling. The effects on both surface wind components amount to a correlation of −0.5 with $\mathbf{u}_a$ at ~34°N at the coast (Fig. S4). By contrast, the northward shift of the high pressure cell is associated with northerly wind anomalies between 45° and 55°N (Fig. 3c) and westerly wind anomalies between 50° and 55°N at the coast (Fig. 4c) with a correlation value of about −0.5 around 50°N, 125°W (Fig. 3c), both of which are favorable for upwelling. In total, the meridional position of the high pressure cell has a significant correlation with $\mathbf{u}_a$ between 42° and 58°N with a maximum value of 0.6 at about 51°N (Fig. S4). These results are consistent with the findings in Schmidt et al. (2020).

We now turn to the ω500 metric. Figure 3d shows that the strength of the NPH-related subsidence is highly correlated with northerly wind anomalies along the west coast with correlation values of −0.6 to −0.7 between 35° and 42°N. Furthermore, the strength is also highly correlated (~0.5) with westerly wind anomalies at about 40°N (Fig. 4d), although the zonal wind has little effect on upwelling given that the coast is nearly meridional at this latitude. The two effects amount to a correlation value of more than 0.7 with $\mathbf{u}_a$ at about 38°N (Fig. S4). The eastward shift of the subsidence induces southerly wind anomalies between 26° and 32°N (Fig. 3e), but the impact of the shift on surface zonal winds is negligible (Fig. 4e). The longitude component of the ω500 metric has an anomaly correlation of approximately −0.4 with $\mathbf{u}_a$ from 26° to 32°N (Fig. S4). The northward shift of the subsidence is associated with northerly wind anomalies (Fig. 3f) and westerly wind anomalies (Fig. 4f) with the maximum correlation value of about −0.5 (Fig. 3f) and 0.5 (Fig. 4f) at ~50°N, both of which are favorable for upwelling. The latitude component of the ω500 metric has significant anomaly correlations (0.4–0.6) with $\mathbf{u}_a$ between 49° and 59°N (Fig. S4).

There are some key differences in the SLP and ω500 NPH metrics, in terms of their relationship to surface winds in the CCS. In particular, the strength of the high pressure cell is

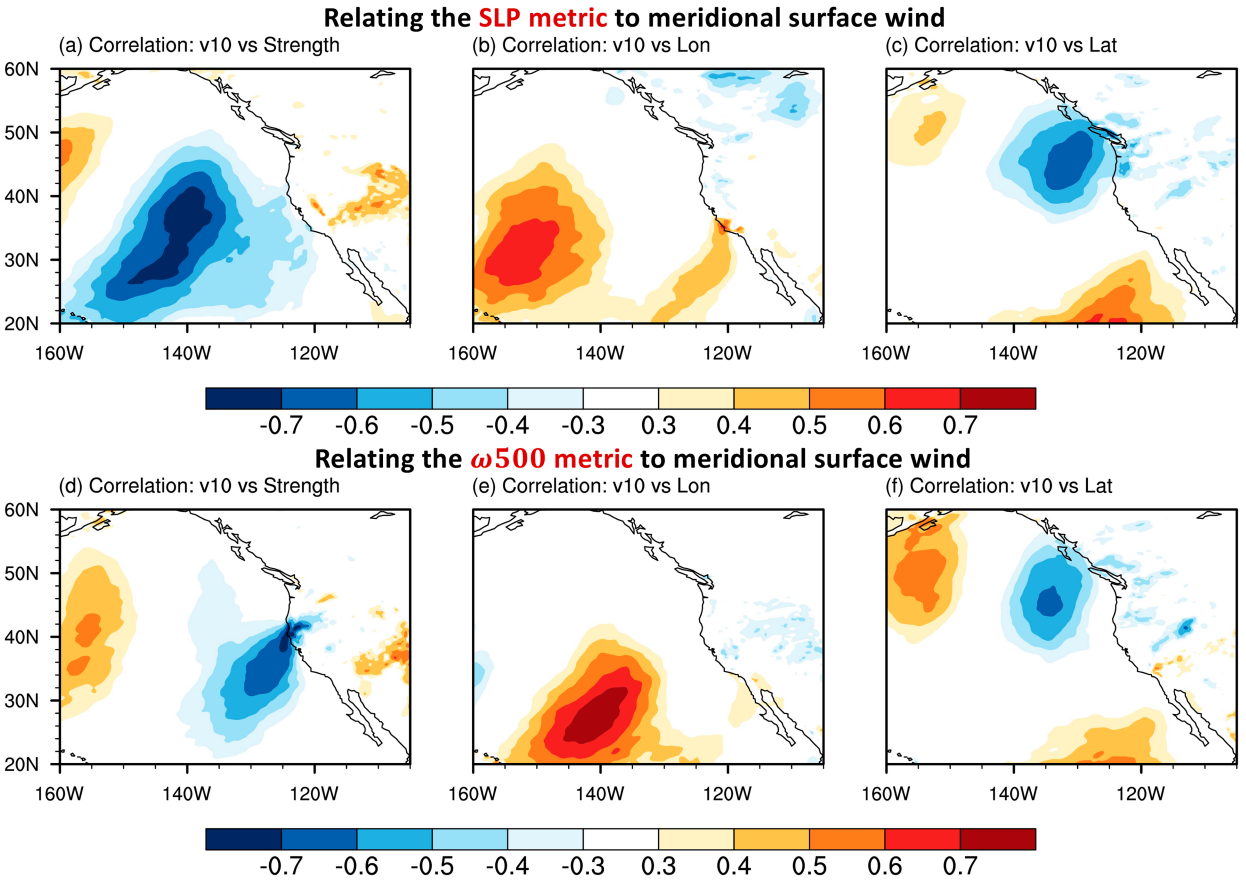

FIG. 3. Anomaly correlation between surface (10-m) meridional wind and the strength, longitude, and latitude of the (a)–(c) SLP metric and (d)–(f) ω500 metric, calculated from the ERA5. Data are detrended prior to calculating the correlation.

marginally related to the winds near the coast, while the subsidence strength explains a substantial fraction (a maximum of 50%) of the coastal wind variability between 35° and 42°N. The strength of the subsidence is highly correlated (0.72) with the maximum $\mathbf{u}_a$. The role of subsidence on upwelling in the CCS has been overlooked in previous studies. The zonal displacements of the high pressure cell and the subsidence affect $\mathbf{u}_a$ at different latitudes (Fig. S4b), while the northward shift of the subsidence affects surface winds in a similar way as that of the high pressure cell as the two latitude components are highly correlated with each other.

We also calculated the correlation between meridional (Fig. 5) and zonal (Fig. S5) wind stress and the three components of the two NPH metrics using the CESM-LE data. The model generally reproduces the impact of the strength components of the two metrics on surface winds in the coastal region as seen by comparing the CESM fields (Figs. 5a,d and Figs. S5a,d) with those from the ERA5 (Figs. 3a,d and 4a,d). For example, the CESM-LE simulates the impact of ω500 strength on the meridional wind around 40°N. However, the effect of the longitude components on the winds is weaker in the model and the placement of the correlation centers differs for some of the metrics. The CESM-LE generally reproduces the latitude component of the SLP metric on the meridional and zonal winds near the coast, although it underestimates the magnitude of the correlations. The latitude component of the ω500 metric in the CESM-LE affects surface winds in different regions than those in ERA5.

c. *The impact of the NPH on coastal winds due to anthropogenic climate change*

The projected changes in SLP are shown in Fig. 6a. SLP increases slightly in response to the external forcing in the middle of the NPH-related high pressure cell between 30° and 40°N, but none of the strength, longitude, or latitude components of the SLP metric changes significantly (Table 1). The high pressure cell shows no obvious displacement in the future climate as shown by the contours of 1020 hPa from the historical and RCP8.5 experiments. The NPH does expand slightly along its northern and southern flanks, but the two contours are nearly coincident with each other along its eastern flank, indicating that the high pressure cell does not change along the west coast of North America. Surprisingly, SLP is projected to increase significantly in the western part of North America. The increased SLP even reduces the sea–land SLP gradient between 20° and 45°N, although the surface air temperature is projected to increase more over the continent than the ocean (not shown). Future changes in surface

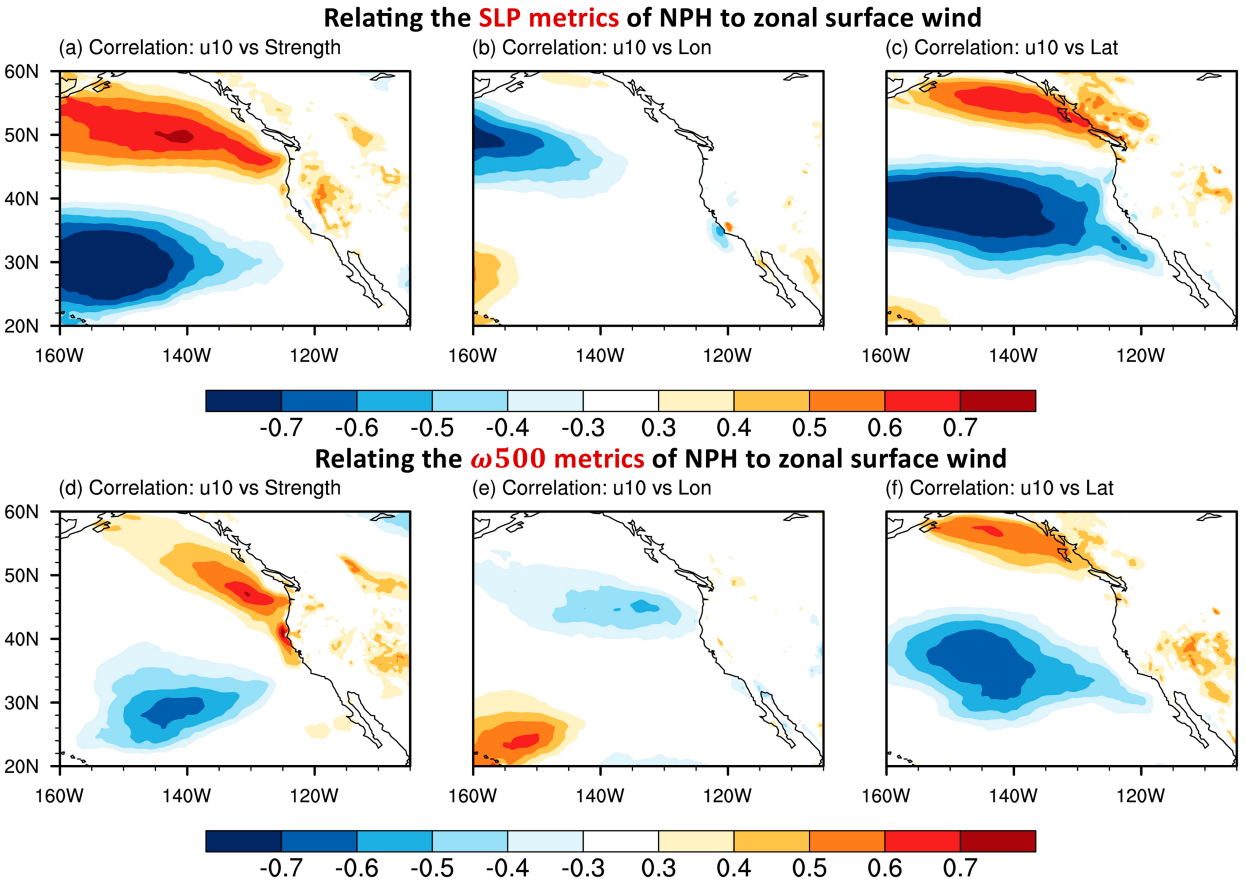

FIG. 4. Anomaly correlation between surface (i.e., 10-m) zonal wind and the strength, longitude, and latitude of the (a)–(c) SLP metric and (d)–(f) ω500 metric, calculated from the ERA5. Data are detrended prior to calculating correlation.

pressure closely resemble those in SLP, including an increase in pressure over western North America (not shown).

The projected changes in SLP, calculated from the CESM2-LE, are shown in Fig. 6b. In general, the CESM2-LE exhibits changes consistent with those in the CESM-LE (Fig. 6a), especially near the west coast of North America. For example, the SLP increases significantly over the northern and southern parts of the eastern North Pacific, but with little or no increase in between, similar to the CESM-LE, indicating similar changes in the SLP gradient between the two models in the eastern North Pacific and thus consistent geostrophic circulation near the surface. He and Zhou (2022) noted that both the rotational and divergent intensity of NPH are projected to weaken based on multiple scenarios of both CMIP5 and CMIP6 models, which is consistent with our results based on the SLP gradient and omega metrics (see below). There are also similar changes in the position of the subtropical high, as indicated by the dashed and solid lines in Fig. 6. The significant increase in SLP over western North America in the CESM2-LE concurs with CESM-LE. The primary difference in SLP occurs in the central North Pacific, where CESM2-LE exhibits a decrease in pressure, while it slightly increases in CESM-LE.

The mean states over the two epochs and their epoch differences in 500-hPa ω and surface wind stress are shown in Fig. 7. The mean subsidence weakens in the future, but the area of subsidence expands farther north (Figs. 7a,b). Indeed, the projected changes in the 500-hPa ω are characterized by significant negative anomalies of -0.005 Pa s^{-1} (i.e., ascending motion) from about 135°W to the U.S. West Coast and between 30° and 40°N (Fig. 7c), reducing the climatological subsidence (Fig. 1) and weakening NPH in the future. The area with strong subsidence (ω of 0.04 Pa s^{-1}) shrinks zonally and shifts northward, as also indicated by the reduced strength and meridional displacement (2.4°) of the ω500 metric. Near the coast, significant positive anomalies of 0.002–0.005 Pa s^{-1} occur between approximately 48° and 55°N and form a dipole pattern with the negative anomalies of -0.01 Pa s^{-1} located between 30° and 45°N (Fig. 7c). The anomalous subsidence reduces the ascending motion along the west coast of Alaska and Canada (Fig. 1).

The projected surface wind stress changes are characterized by cyclonic (anticyclonic) circulation south (north) of ~45°N (Fig. 7d). A similar circulation change was noted in the CMIP5 multimodel ensemble mean (He et al. 2017). The westward surface wind stress change around 40°–50°N is also consistent with narrowing low-level zonal wind distribution (Brewer and Mass 2016). The Laplacian of SLP, which is an approximation of the rotational wind component, indicates cyclonic and anticyclonic

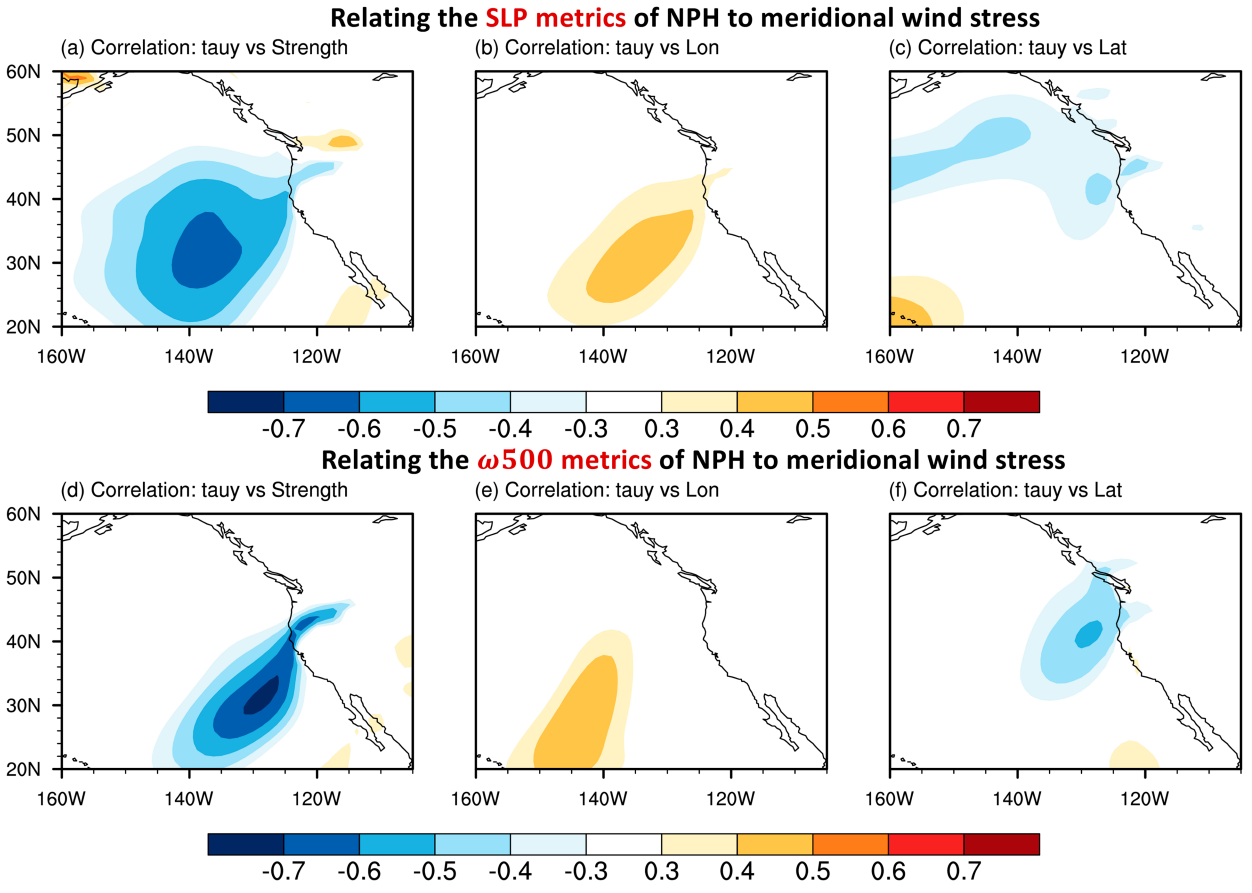

FIG. 5. Anomaly correlation between meridional wind stress and the strength, longitude, and latitude of the (a)–(c) SLP metric and (d)–(f) ω500 metric, calculated from the CESM-LE. Data are detrended prior to calculating the correlation.

circulation changes in the southern and northern part of the eastern North Pacific, respectively (not shown), consistent with the changes in surface wind stress. On the eastern flank of the anomalous cyclone, poleward surface wind stress anomalies occur near the California coast, reducing the climatological mean $\boldsymbol{\tau}_a$ there (Figs. 1 and 7a). Like $\mathbf{u}_a$, $\boldsymbol{\tau}_a$ is calculated by projecting zonal and meridional wind stress from the first offshore grid cells onto the estimate of the angle of the coastline. This weakening of $\boldsymbol{\tau}_a$ is related to the weaker-than-normal NPH-related subsidence above (Fig. 7c) consistent with the Sverdrup balance. Likewise, the intensification of $\boldsymbol{\tau}_a$ north of ~45°N is also associated with the anomalous descent in the northeastern North Pacific. The area of surface wind stress that is directed toward the southeast expands slightly north extending along the coastal to 55°N (Fig. 7b). The surface westerly changes in this area were

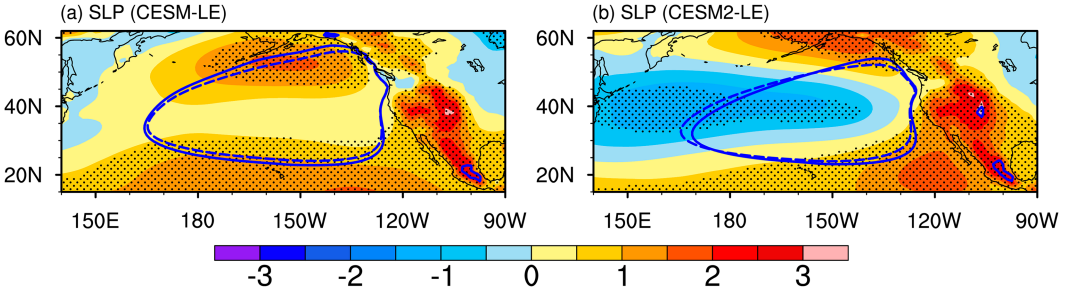

FIG. 6. The epoch difference (2071–2100 minus 1925–54) in SLP, calculated from (a) CESM-LE and (b) CESM2-LE. Dots indicate 95% confidence level where the signal-to-noise ratio ≥2; dashed and solid lines show the contours of 1020 hPa for summer mean calculated over the years 1925–54 and 2071–2100, respectively. The units in each panel are hPa.

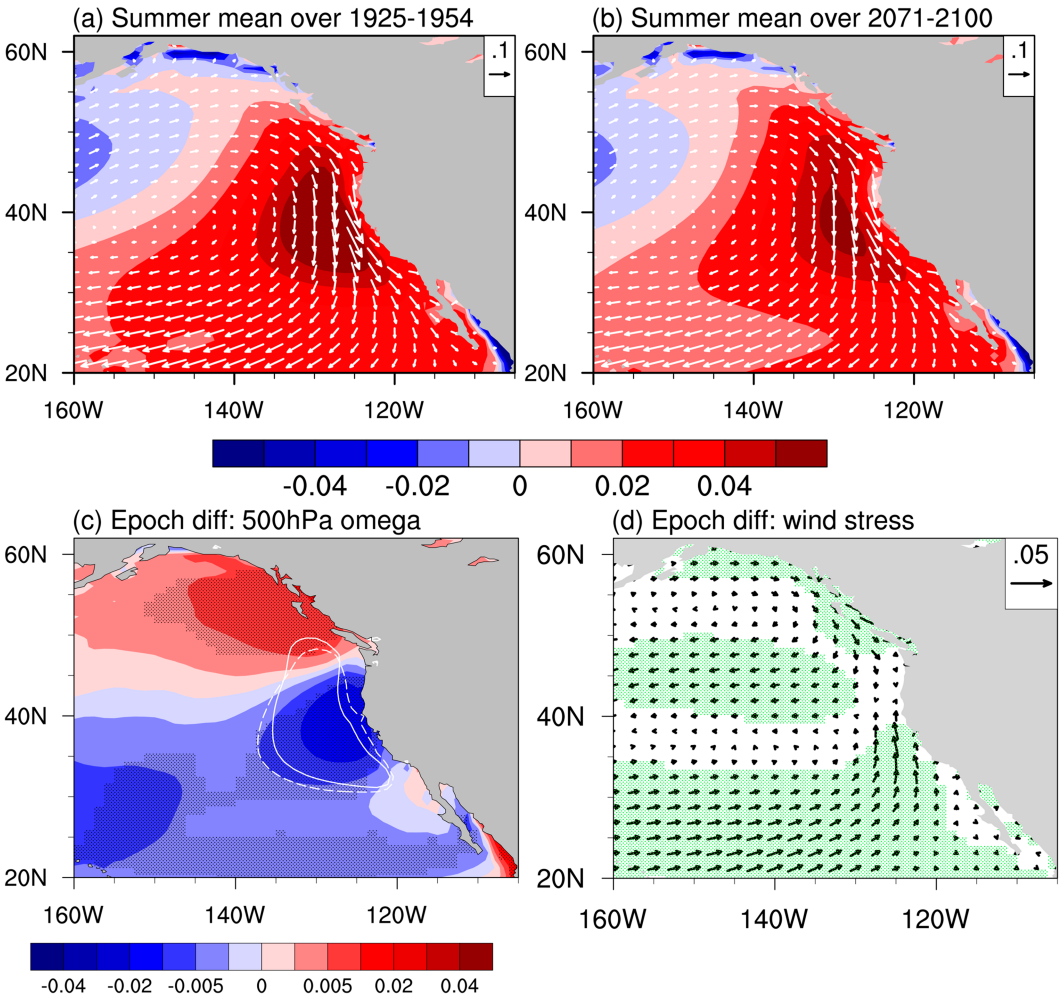

FIG. 7. Summer mean 500-hPa pressure vertical velocity (shading) and surface wind stress (vectors) over (a) 1925–54 and (b) 2071–2100 and the epoch difference (2071–2100 minus 1925–54) in (c) the 500-hPa pressure vertical velocity and (d) the surface wind stress. Dots in (c) and green shading in (d) indicate 95% significance. In (c), dashed and solid lines show the contours of 0.04 Pa s^{-1} for summer means calculated over the years 1925–54 and 2071–2100, respectively. The units for vertical pressure velocity and wind stress are Pa s^{-1} and N m^{-2}, respectively.

also noted by Mass et al. (2022) using a high-resolution regional model simulation.

We used the CESM2-LE to test the robustness of future changes in the vertical velocity and surface wind stress. The projected changes in 500-hPa ω and surface wind stress in the CESM2-LE (Figs. 8c,d) closely resemble those in the CESM-LE (Figs. 7c,d). The projected changes in the 500-hPa ω are characterized by significant negative anomalies of -0.01 Pa s^{-1} (i.e., ascending motion) near the California coast between 30° and 40°N (Fig. 8c), reducing the climatological subsidence there (Fig. 8a). Accordingly, northward surface wind stress changes occur along the coast (Fig. 8d), which are unfavorable for upwelling as in the CESM-LE (Fig. 7d). One difference from the CESM-LE is that the NPH-related subsidence weakens over a larger area in the CESM2-LE. Accordingly, northward surface wind stress changes are also stronger than in the CESM-LE near the California coast. Significant positive anomalies of 0.002–0.005 Pa s^{-1} occur near the coast north of ~48°N, which reduces the climatological ascending motion along the west coast of Alaska and Canada (Fig. 8a), consistent with those in the CESM-LE (Fig. 7c). The southeastward surface wind stress changes also occur along the coast in the CESM2-LE, but are weaker than those in the CESM-LE. The difference from the CESM-LE is associated with a smaller area with anomalous subsidence in the Gulf of Alaska in the CESM2-LE compared to the CESM-LE.

The link between the forced changes in 500-hPa pressure vertical velocity and meridional wind are illustrated in Fig. 9a using a height and latitude cross section along the west coast of North America. Southerly wind and ascending anomalies are located between 32° and 40°N. Farther north, northerly wind and descending anomalies occur from 43° to 59°N. Together they form an anomalous clockwise circulation, where $\boldsymbol{\tau}_a$ is weakened (strengthened) in the southern (northern) part of the domain (Fig. 9b). In general, the interface between

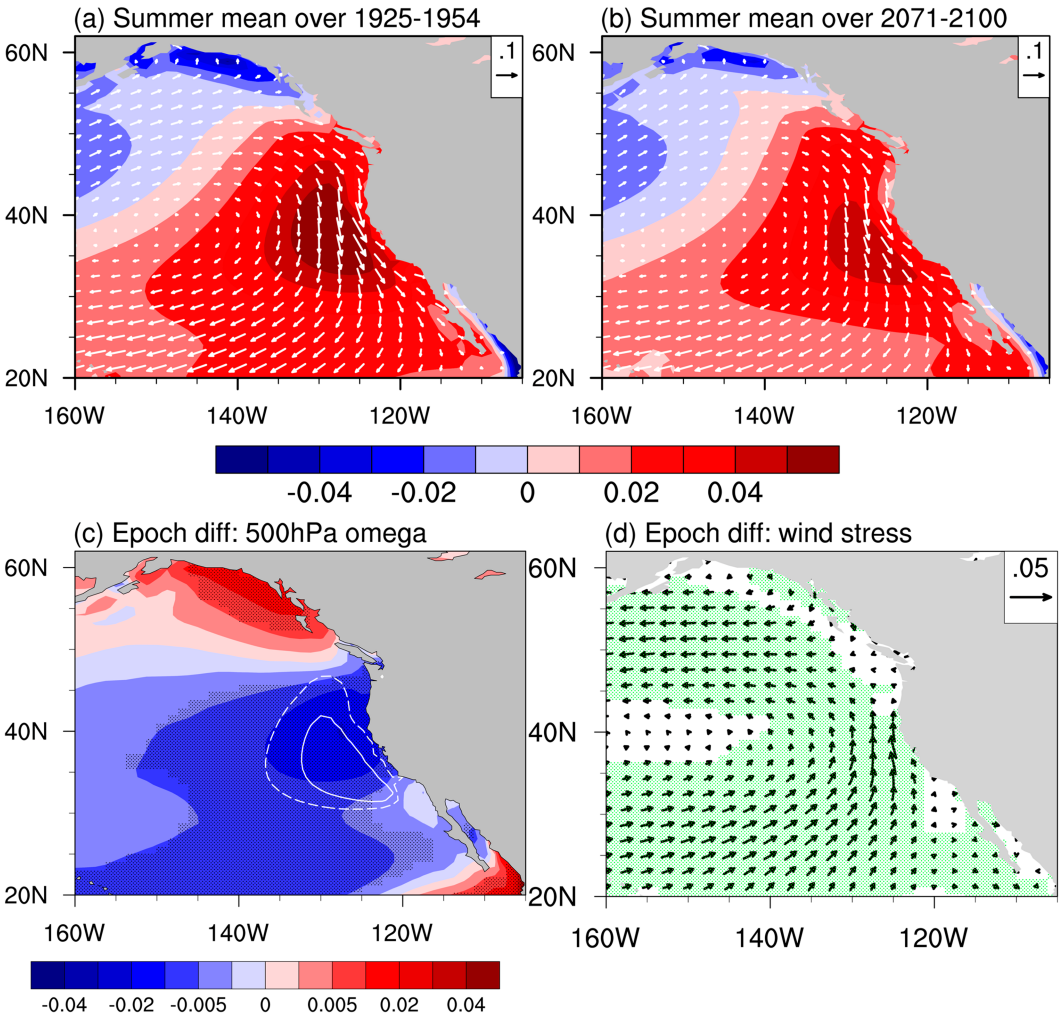

FIG. 8. As in Fig. 7, but using the CESM2-LE.

weakened and intensified τ_a in the anomalous clockwise circulation is approximately located at 42°N. In addition, there is another interface in the south around 29°N for opposite changes in τ_a. Figure 9c shows the percentage of forced changes in τ_a relative to the summer mean state calculated from the first epoch over the years 1925–54. At 23°–24°N, τ_a increases by about 8%. Near the Californian coast between 34° and 39°N, τ_a weakens by 10%–12%. To the north of 47°N, τ_a changes significantly toward being favorable for coastal upwelling, and the percentage increases from 10% around 47°N to 150% around 59°N (Fig. 9c). Farther north, the percentage is about 150%, but with the opposite sign. These large percentage changes result from the mean τ_a being close to zero near the northern part of the domain. An examination of the zonal and meridional components of wind stress indicates that both components change significantly along the North American west coast (not shown).

We further examine the link between the externally forced changes in 500-hPa pressure vertical velocity and τ_a using the 40 independent members in the CESM-LE. A scatterplot of the epoch differences of the strength component of the ω500 metric (abscissa) and τ_a (ordinate) averaged over latitudes of 34.5° and 40.5°N for all ensemble members is shown in Fig. 10a; τ_a displays significant weakening over this latitude range (Fig. 9b). All members show reduced subsidence and τ_a (negative values for both) in a changing climate. There is a clear linear relationship between the two quantities with an intermember correlation value of 0.75, which is significant at the 95% confidence level. The linear relationship suggests that a decrease in subsidence leads to a proportional decrease in τ_a. The correlation value of 0.75 indicates that about 60% of changes in τ_a are explained by changes in the NPH-related subsidence. The relationship between the epoch differences in τ_a and the position components of the ω500 metric was also examined, but no significant relationship was found (not shown). The anomalous subsidence in the north part of the domain is strongly related to the intensification of τ_a along the west coast of Canada and Alaska (Fig. 10b). The intermember correlation is 0.87, suggesting that about 70% intensification of τ_a is due to the anomalous subsidence above.

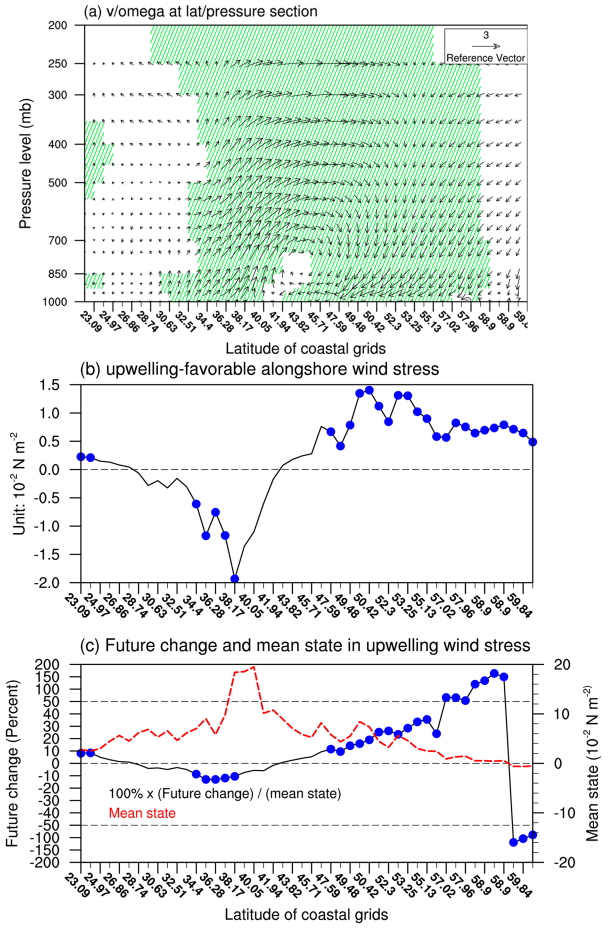

FIG. 9. Epoch difference (2071–2100 minus 1925–54) in the CESM-LE (a) meridional wind (v) and pressure vertical velocity (omega) in pressure and latitude cross section along the west coast of North America and (b) upwelling-favorable alongshore wind stress and (c) the mean state (1925–54; right axis) and percent future change (2071–2100; left axis) of upwelling-favorable alongshore wind stress. Hatching in (a) and dots in (b) and (c) indicate 95% significance. In (a), the changes in omega are scaled by $-1 \times$ [max value(changes of$v$)/max value(changes of omega)].

d. The possible mechanism for future changes in the NPH

Using multimodel CMIP5 simulations, He et al. (2017) also found that the summer NPH displayed significant changes in response to greenhouse gas forcing, including anomalous ascent/cyclone in the southern and anomalous descent/anticyclone in the northern part of the North Pacific. They suggested that the changes in the NPH were due to the combined effects of increased tropospheric static stability and changes in diabatic heating by conducting numerical simulations using a simple atmospheric model, consistent with forced changes in precipitation inducing significant changes in ω in the future (Nie et al. 2018). The response of the atmospheric model to increased static stability featured a cyclone and an anticyclone in the subtropical and northern North Pacific, respectively. The model also displayed an anticyclonic response in the North Pacific to the changes in diabatic heating, which were dominated by positive heating anomalies in the northwestern tropical Pacific and negative anomalies in the North Atlantic. Wills et al. (2019) found weakening of both descent and ascent at 500 hPa in the Northern Hemisphere and tropics in response to greenhouse gas forcing in CMIP5 simulations. This included reduced descent and ascent in the southern and the northern part of the eastern North Pacific, respectively. They ascribed the slowing down of vertical velocity to decreased global convective mass flux due to a slower increase of precipitation compared with faster increase of water vapor in the atmosphere (Vecchi and Soden 2007). A third possible explanation for the changes in midtroposphere ω result from externally forced changes in the upper troposphere (Blackmon et al. 1977). Figure 11a shows the greenhouse gas–forced changes in 250-hPa atmospheric circulation, which tend to weaken the summer westerly jet in the subtropical North Pacific (Fig. S6b). The deceleration is likely due to the reduced meridional temperature gradient (e.g., Coumou et al. 2018). The anomalous anticyclonic circulation over the Columbia River basin in Fig. 11a was also noted by Rupp et al. (2017) based on the CMIP5 multimodel ensemble mean. The changes in the atmospheric circulation at 250 hPa are associated with anomalous divergence around 40°N near the California coast and anomalous convergence farther north near the Canadian west coast (Fig. 11b), consistent with weakened subsidence and ascent below in the midtroposphere (Fig. 7c). Figure 11b also indicates that the greenhouse gas–forced changes are nearly opposite to and thus weaken the climatological mean state (i.e., contours). It is worth noting that the CESM-LE represents the westerly jet at 250 hPa reasonably well (Fig. S6). In addition to the differing hypotheses for changes in the NPH, a consensus has not been reached on how it may evolve in the future. For example, Li et al. (2012) found that the NPH-related anticyclone in the lower troposphere would intensify in the future, attributing the response to increased land–sea thermal contrasts and corresponding changes in diabatic heating.

Several recent studies noted that the NPH exhibits a distinct response to global warming compared with the North Atlantic subtropical high (NAH), which was attributed to the asymmetric continental distribution between the Eastern and Western Hemispheres and the change in SST pattern (Shaw and Voigt 2015; He and Zhou 2022). The associated change in surface winds over the North Atlantic could impact coastal upwelling associated with the Canary Current (e.g., Rykaczewski et al. 2015; Wang et al. 2015).

4. Summary and discussion

In this study, we have examined the influence of the North Pacific high (NPH) on surface winds in the North Pacific eastern boundary in summer (JJA), the primary upwelling season. In addition to defining a SLP metric to measure the NPH-related surface high pressure cell, we also defined an ω500 metric to represent the NPH-related large-scale subsidence with the maximum occurring in the eastern boundary region (Fig. 1; Seager et al. 2003). This is because the subsidence is related to meridional wind according to Sverdrup balance (Rodwell and Hoskins 2001),

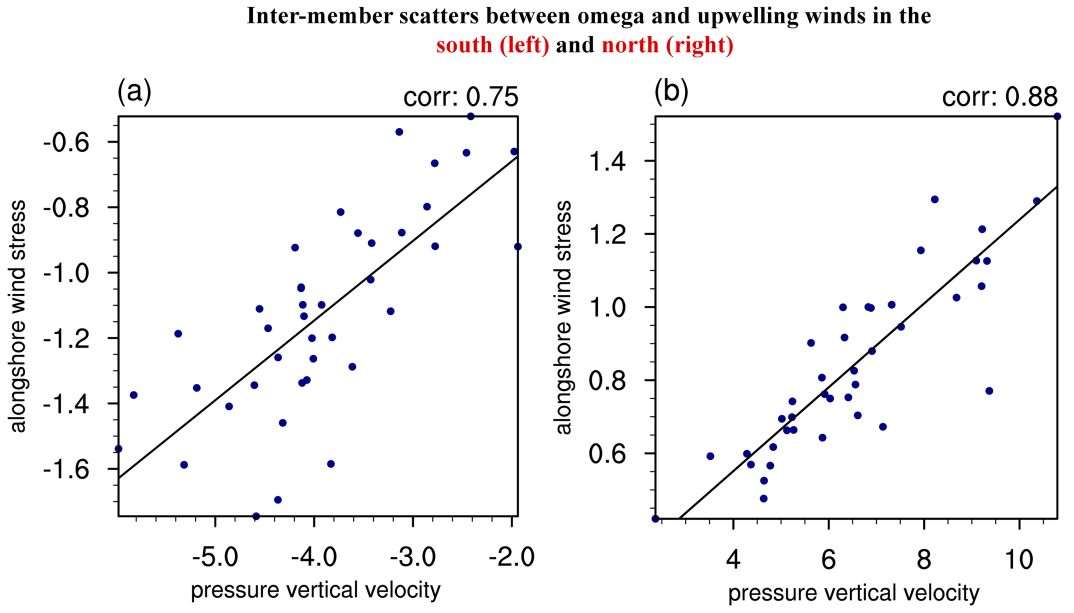

FIG. 10. Scatterplots between summer (JJA) epoch difference in upwelling-favorable alongshore wind stress (ordinate) and the epoch difference in the CESM-LE for (a) the strength of the $\omega 500$ metric and (b) the 500-hPa pressure vertical velocity averaged in the domain bounded by 48°–58°N, 140°–127°W. The upwelling-favorable alongshore wind stress is averaged at latitudes of (a) 34°–38°N and (b) 48°–60°N. The units for abscissa (x axis) and ordinate (y axis) are 10^{-3} Pa s^{-1} and 10^{-2} N m^{-2}, respectively.

and the meridional wind is the primary component of winds that induce coastal upwelling. Further, the effect of the descent has not been examined in previous studies of the influence of the NPH on coastal upwelling.

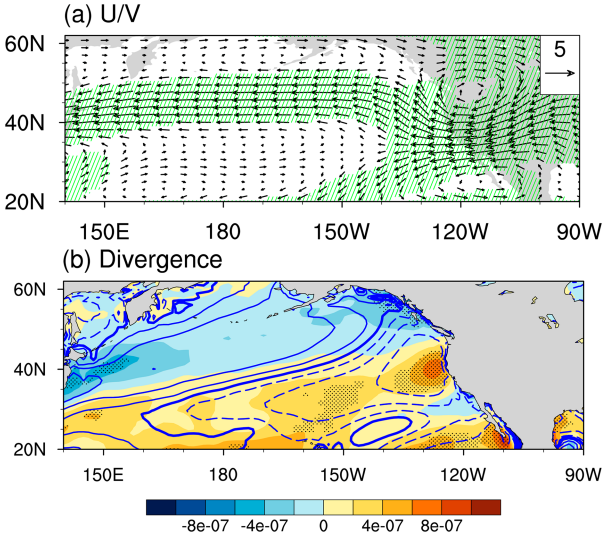

FIG. 11. Epoch difference (2071–2100 minus 1925–54) in the CESM-LE (a) wind fields and (b) divergence at 250 hPa. Green shading in (a) and dots in (b) indicate 95% significance. In (b), the summer mean 250-hPa divergence over 1925–2917 is shown by blue contours at $(-3, -2, -1, -0.5, -0.2, 0, 0.2, 0.5, 1, 2, 3) \times 10^{-6}$. Positive and negative contours are shown by solid and dashed lines, respectively, while zero line is the thickness line. The units in (a) and (b) are m s^{-1} and m s^{-2}, respectively.

The NPH-related high pressure cell and subsidence, as measured by their strength, longitude, and latitude, both affect upwelling-favorable alongshore surface winds ($\mathbf{u}_a$). The key difference is that the strength component of the $\omega 500$ metric is strongly correlated to $\mathbf{u}_a$ near California coast while that of the SLP metric is only marginally related to $\mathbf{u}_a$. Both the longitude components of the two metrics are related to $\mathbf{u}_a$ along the southern California coast, but at different latitudes. The latitude components of the two metrics exert similar impacts on $\mathbf{u}_a$ along the west coast of Canada and Alaska. A likely mechanism is that the subsidence adds atmospheric mass to the high pressure cell and thus the meridional shift of the subsidence induces the same meridional displacement of the high pressure cell (not shown).

The NPH-related surface high pressure cell and subsidence exhibit distinct changes in response to greenhouse gas forcing according to the CESM-LE. The three components of the SLP metric change only slightly in the future climate (Table 1). By contrast, the subsidence is substantially reduced (Table 1), which contributes to the reduction in $\boldsymbol{\tau}_a$ near the California coast consistent with Sverdrup balance. Further, the uncertainty of future change in the subsidence is also consistent with the uncertainty in the change of $\boldsymbol{\tau}_a$ in the future climate, which is indicated by an intermember correlation value of 0.75 between them. The intermember spread of future changes in the subsidence is likely associated with the interdecadal Pacific oscillation/Pacific decadal oscillation (Johnson et al. 2020) low-frequency fluctuations internal to the climate system. Note that $\boldsymbol{\tau}_a$ intensifies along the west coast of Canada and Alaska, which is largely due to the weakened ascent in the northeast Pacific. The intermember correlation between the

anomalous subsidence and intensified τ_a reaches 0.87, suggesting that the anomalous subsidence explains 75% of the change in τ_a in the northern part of the west coast of North America. The future changes in the NPH-related subsidence and its effect on τ_a along the North America west coast, obtained from the CESM-LE, have been largely confirmed by 80 independent ensemble members from the CESM2 large ensemble.

Both the SLP and surface pressure over the western United States increase considerably in response to greenhouse gas forcing in both the CESM and CESM2 large ensembles, which in turn, weakens the mean land–sea pressure gradient. This is opposite to the Bakun (1990) hypothesis. Rykaczewski et al. (2015) also find limited evidence for intensified sea–land cross-shore pressure gradient in response to increasing land–sea temperature differences in the future using multiple CMIP5 models. Changes in water vapor also influence SLP and water vapor content is projected to increase in response to greenhouse gas forcing (Yang et al. 2016). Indeed, the water vapor content significantly increases globally in the CESM-LE (not shown). Changes in SLP over the continent and the reason why it occurs, including changes in water vapor, warrant further examination. In addition, while previous studies have examined greenhouse gas–driven changes in the four EBUSs (e.g., Rykaczewski et al. 2015; Wang et al. 2015), comparative analyses across systems, including the role of subsidence, may enhance our understanding of the key processes driving changes in upwelling.

Acknowledgments. This work has been funded by the NOAA Earth System Modeling program. We acknowledge the NCAR climate modeling group for producing and making available their model output.

Data availability statement. The ERA5 data are available at https://rda.ucar.edu/datasets/ds630.0/. The CESM-LE data are available at https://www.earthsystemgrid.org/dataset/ucar.cgd.ccsm4.CESM_CAM5_BGC_LE.html. The CESM2-LE data are available at https://www.earthsystemgrid.org/dataset/ucar.cgd.cesm2le.output.html.

REFERENCES

Bakun, A., 1973: Coastal upwelling indices, west coast of North America, 1946–71. NOAA Tech. Rep. NMFS-SSRF-671, 112 pp., https://spo.nmfs.noaa.gov/SSRF/SSRF671.pdf.

——, 1975: Daily and weekly upwelling indices, west coast of North America, 1967–73. NOAA Tech. Rep. NMFS SSRF-693, 124 pp., https://repository.library.noaa.gov/view/noaa/15387.

——, 1990: Global climate change and intensification of coastal ocean upwelling. *Science*, **247**, 198–201, https://doi.org/10.1126/science.247.4939.198.

Belmadani, A., V. Echevin, F. Codron, K. Takahashi, and C. Junquas, 2014: What dynamics drive future wind scenarios for coastal upwelling off Peru and Chile? *Climate Dyn.*, **43**, 1893–1914, https://doi.org/10.1007/s00382-013-2015-2.

Blackmon, M. L., J. M. Wallace, N.-C. Lau, and S. L. Mullen, 1977: An observational study of the Northern Hemisphere wintertime circulation. *J. Atmos. Sci.*, **34**, 1040–1053, https://doi.org/10.1175/1520-0469(1977)034<1040:AOSOTN>2.0.CO;2.

Brady, R. X., M. A. Alexander, N. S. Lovenduski, and R. R. Rykaczewski, 2017: Emergent anthropogenic trends in California Current upwelling. *Geophys. Res. Lett.*, **44**, 5044–5052, https://doi.org/10.1002/2017GL072945.

Brewer, M. C., and C. F. Mass, 2016: Projected changes in heat extremes and associated synoptic- and mesoscale conditions over the northwest United States. *J. Climate*, **29**, 6383–6400, https://doi.org/10.1175/JCLI-D-15-0641.1.

Chhak, K., and E. Di Lorenzo, 2007: Decadal variations in the California Current upwelling cells. *Geophys. Res. Lett.*, **34**, L14604, https://doi.org/10.1029/2007GL030203.

Coumou, D., G. Di Capua, S. Vavrus, L. Wang, and S. Wang, 2018: The influence of Arctic amplification on mid-latitude summer circulation. *Nat. Commun.*, **9**, 2959, https://doi.org/10.1038/s41467-018-05256-8.

Danabasoglu, G., and Coauthors, 2020: The Community Earth System Model version 2 (CESM2). *J. Adv. Model. Earth Syst.*, **12**, e2019MS001916, https://doi.org/10.1029/2019MS001916.

Deser, C., A. S. Phillips, M. A. Alexander, and B. V. Smoliak, 2014: Projecting North American climate over the next 50 years: Uncertainty due to internal variability. *J. Climate*, **27**, 2271–2296, https://doi.org/10.1175/JCLI-D-13-00451.1.

——, L. Terray, and A. S. Phillips, 2016: Forced and internal components of winter air temperature trends over North America during the past 50 years: Mechanisms and implications. *J. Climate*, **29**, 2237–2258, https://doi.org/10.1175/JCLI-D-15-0304.1.

Ding, H., M. A. Alexander, and M. G. Jacox, 2021: Role of geostrophic currents in future changes of coastal upwelling in the California Current system. *Geophys. Res. Lett.*, **48**, e2020GL090768, https://doi.org/10.1029/2020GL090768.

García-Reyes, M., and J. Largier, 2010: Observations of increased wind-driven coastal upwelling off central California. *J. Geophys. Res.*, **115**, C04011, https://doi.org/10.1029/2009JC005576.

——, W. J. Sydeman, B. A. Black, R. R. Rykaczewski, D. S. Schoeman, S. J. Thompson, and S. A. Bograd, 2013: Relative influence of oceanic and terrestrial pressure systems in driving upwelling-favorable winds. *Geophys. Res. Lett.*, **40**, 5311–5315, https://doi.org/10.1002/2013GL057729.

——, ——, D. S. Schoeman, R. R. Rykaczewski, B. A. Black, A. J. Smit, and S. J. Bograd, 2015: Under pressure: Climate change, upwelling, and eastern boundary upwelling ecosystems. *Front. Mar. Sci.*, **2**, 109, https://doi.org/10.3389/fmars.2015.00109.

He, C., and T. Zhou, 2022: Distinct responses of North Pacific and North Atlantic summertime subtropical anticyclones to global warming. *J. Climate*, **35**, 8117–8132, https://doi.org/10.1175/JCLI-D-21-1024.1.

——, B. Wu, L. Zou, and T. Zhou, 2017: Responses of the summertime subtropical anticyclones to global warming. *J. Climate*, **30**, 6465–6479, https://doi.org/10.1175/JCLI-D-16-0529.1.

Hersbach, H., and Coauthors, 2020: The ERA5 global reanalysis. *Quart. J. Roy. Meteor. Soc.*, **146**, 1999–2049, https://doi.org/10.1002/qj.3803.

Hoskins, B., M. Pedder, and D. W. Jones, 2003: The omega equation and potential vorticity. *Quart. J. Roy. Meteor. Soc.*, **129**, 3277–3303, https://doi.org/10.1256/qj.02.135.

Hsieh, W., and G. J. Boer, 1992: Global climate change and ocean upwelling. *Fish. Oceanogr.*, **1**, 333–338, https://doi.org/10.1111/j.1365-2419.1992.tb00005.x.

Huyer, A., 1983: Coastal upwelling in the California Current system. *Prog. Oceanogr.*, **12**, 259–284, https://doi.org/10.1016/0079-6611(83)90010-1.

Jacox, M. G., C. A. Edwards, E. L. Hazen, and S. J. Bograd, 2018: Coastal upwelling revisited: Ekman, Bakun, and improved upwelling indices for the U.S. West Coast. *J. Geophys. Res. Oceans*, **123**, 7332–7350, https://doi.org/10.1029/2018JC014187.

Johnson, N. C., D. J. Amaya, Q. Ding, Y. Kosaka, H. Tokinaga, and S.-P. Xie, 2020: Multidecadal modulations of key metrics of global climate change. *Global Planet. Change*, **188**, 103149, https://doi.org/10.1016/j.gloplacha.2020.103149.

Karnauskas, K. B., and C. C. Ummenhofer, 2014: On the dynamics of the Hadley circulation and subtropical drying. *Climate Dyn.*, **42**, 2259–2269, https://doi.org/10.1007/s00382-014-2129-1.

Kay, J. E., and Coauthors, 2015: The Community Earth System Model (CESM) large ensemble project: A community resource for studying climate change in the presence of internal climate variability. *Bull. Amer. Meteor. Soc.*, **96**, 1333–1349, https://doi.org/10.1175/BAMS-D-13-00255.1.

Li, W., L. Li, M. Ting, and Y. Liu, 2012: Intensification of Northern Hemisphere subtropical highs in a warming climate. *Nat. Geosci.*, **5**, 830–834, https://doi.org/10.1038/ngeo1590.

Liu, Y., G. Wu, and R. Ren, 2004: Relationship between the subtropical anticyclone and diabatic heating. *J. Climate*, **17**, 682–698, https://doi.org/10.1175/1520-0442(2004)017<0682:RBTSAA>2.0.CO;2.

Loikith, P. C., D. Singh, and G. P. Taylor, 2022: Projected changes in atmospheric ridges over the Pacific–North American region using CMIP6 models. *J. Climate*, **35**, 5151–5171, https://doi.org/10.1175/JCLI-D-21-0794.1.

Lovenduski, N. S., G. A. McKinley, A. R. Fay, K. Lindsay, and M. C. Long, 2016: Partitioning uncertainty in ocean carbon uptake projections: Internal variability, emission scenario, and model structure. *Global Biogeochem. Cycles*, **30**, 1276–1287, https://doi.org/10.1002/2016GB005426.

Manabe, S., R. J. Stouffer, M. J. Spelman, and K. Bryan, 1991: Transient responses of a coupled ocean–atmosphere model to gradual changes of atmospheric CO_2. Part I. Annual mean response. *J. Climate*, **4**, 785–818, https://doi.org/10.1175/1520-0442(1991)004<0785:TROACO>2.0.CO;2.

Mann, K. H., and J. R. Lazier, 2013: *Dynamics of Marine Ecosystems: Biological–Physical Interactions in the Oceans*. John Wiley and Sons, 512 pp.

Mass, C. F., E. P. Salathe Jr., R. Steed, and J. Baars, 2022: The mesoscale response to global warming over the Pacific Northwest evaluated using a regional climate model ensemble. *J. Climate*, **35**, 2035–2053, https://doi.org/10.1175/JCLI-D-21-0061.1.

Miyasaka, T., and H. Nakamura, 2005: Structure and formation mechanisms of the Northern Hemisphere summertime subtropical highs. *J. Climate*, **18**, 5046–5065, https://doi.org/10.1175/JCLI3599.1.

Mote, P. W., and N. J. Mantua, 2002: Coastal upwelling in a warmer future. *Geophys. Res. Lett.*, **29**, 2138, https://doi.org/10.1029/2002GL016086.

Narayan, N., A. Paul, S. Mulitza, and M. Schulz, 2010: Trends in coastal upwelling intensity during the late 20th century. *Ocean Sci.*, **7**, 815–823, https://doi.org/10.5194/os-6-815-2010.

Nie, J., A. H. Sobel, D. A. Shaevitz, and S. Wang, 2018: Dynamic amplification of extreme precipitation sensitivity. *Proc. Natl. Acad. Sci. USA*, **115**, 9467–9472, https://doi.org/10.1073/pnas.1800357115.

Riahi, K., and Coauthors, 2011: RCP 8.5—A scenario of comparatively high greenhouse gas emissions. *Climate Dyn.*, **109**, 33–57, https://doi.org/10.1007/s10584-011-0149-y.

Richter, I., 2015: Climate model biases in the eastern tropical oceans: Causes, impacts and ways forward. *Wiley Interdiscip. Rev.: Climate Change*, **6**, 345–358, https://doi.org/10.1002/wcc.338.

Rodwell, M. J., and B. J. Hoskins, 2001: Subtropical anticyclones and summer monsoons. *J. Climate*, **14**, 3192–3211, https://doi.org/10.1175/1520-0442(2001)014<3192:SAASM>2.0.CO;2.

Rupp, D. E., J. T. Abatzoglou, and P. W. Mote, 2017: Projections of 21st century climate of the Columbia River Basin. *Climate Dyn.*, **49**, 1783–1799, https://doi.org/10.1007/s00382-016-3418-7.

Rykaczewski, R. R., J. P. Dunne, W. J. Sydeman, M. García-Reyes, B. A. Black, and S. J. Bograd, 2015: Poleward displacement of coastal upwelling-favorable winds in the ocean's eastern boundary currents through the 21st century. *Geophys. Res. Lett.*, **42**, 6424–6431, https://doi.org/10.1002/2015GL064694.

Schmidt, D. F., D. J. Amaya, K. M. Grise, and A. J. Miller, 2020: Impacts of shifting subtropical highs on the California Current and Canary Current systems. *Geophys. Res. Lett.*, **47**, e2020GL088996, https://doi.org/10.1029/2020GL088996.

Schroeder, I. D., B. A. Black, W. J. Sydeman, S. J. Bograd, E. L. Hazen, J. A. Santora, and B. K. Wells, 2013: The North Pacific High and wintertime pre-conditioning of California current productivity. *Geophys. Res. Lett.*, **40**, 541–546, https://doi.org/10.1002/grl.50100.

Seager, R., R. Murtugudde, N. Naik, A. Clement, N. Gordon, and J. Miller, 2003: Air–sea interaction and the seasonal cycle of the subtropical anticyclones. *J. Climate*, **16**, 1948–1966, https://doi.org/10.1175/1520-0442(2003)016<1948:AIATSC>2.0.CO;2.

Shaw, T. A., and A. Voigt, 2015: Tug of war on summertime circulation between radiative forcing and sea surface warming. *Nat. Geosci.*, **8**, 560–566, https://doi.org/10.1038/ngeo2449.

Sydeman, W. J., M. García-Reyes, D. S. Schoeman, R. R. Rykaczewski, S. A. Thompson, B. A. Black, and S. J. Bograd, 2014: Climate change and wind intensification in coastal upwelling ecosystems. *Science*, **345**, 77–80, https://doi.org/10.1126/science.1251635.

Vecchi, G. A., and B. J. Soden, 2007: Global warming and the weakening of the tropical circulation. *J. Climate*, **20**, 4316–4340, https://doi.org/10.1175/JCLI4258.1.

Wang, D., T. C. Gouhier, B. A. Menge, and A. R. Ganguly, 2015: Intensification and spatial homogenization of coastal upwelling under climate change. *Nature*, **518**, 390–394, https://doi.org/10.1038/nature14235.

Wang, M., J. E. Overland, and N. A. Bond, 2010: Climate projections for selected large marine ecosystems. *J. Mar. Syst.*, **79**, 258–266, https://doi.org/10.1016/j.jmarsys.2008.11.028.

Wills, R. C. J., R. H. White, and X. J. Levine, 2019: Northern Hemisphere stationary waves in a changing climate. *Curr. Climate Change Rep.*, **5**, 372–389, https://doi.org/10.1007/s40641-019-00147-6.

Yang, J., W. R. Peltier, and Y. Hu, 2016: Monotonic decrease of the zonal SST gradient of the equatorial Pacific as a function of CO_2 concentration in CCSM3 and CCSM4. *J. Geophys. Res. Atmos.*, **121**, 10 637–10 653, https://doi.org/10.1002/2016JD025231.